LA-5403-MS

INFORMAL REPORT

c.3

Thermonuclear Burn Characteristics of Compressed Deuterium-Tritium Microspheres

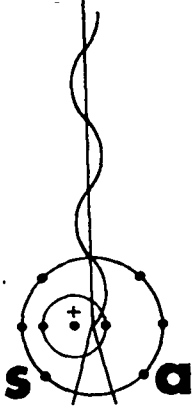

los alamos
scientific laboratory
of the University of California
LOS ALAMOS, NEW MEXICO 87544

UNITED STATES
ATOMIC ENERGY COMMISSION
CONTRACT W-7405-ENG. 36

In the interest of prompt distribution, this LAMS report was not edited by the Technical Information staff.

Printed in the United States of America. Available from
National Technical Information Service
U. S. Department of Commerce
5285 Port Royal Road
Springfield, Virginia 22151
Price: Printed Copy $4.00: Microfiche $0.95

LA-5403-MS
Informal Report
UC-20

ISSUED: October 1973

los alamos
scientific laboratory
of the University of California
LOS ALAMOS, NEW MEXICO 87544

Thermonuclear Burn Characteristics of Compressed Deuterium-Tritium Microspheres

by

G. S. Fraley
E. J. Linnebur
R. J. Mason
R. L. Morse

THERMONUCLEAR BURN CHARACTERISTICS OF COMPRESSED DEUTERIUM-TRITIUM MICROSPHERES

by

G. S. Fraley
E. J. Linnebur
R. J. Mason
R. L. Morse

ABSTRACT

The phenomenology of thermonuclear burn in Deuterium-Tritium microspheres at high densities is described, and numerical results characterizing the burn for a broad range of initial conditions are given. The fractional burn-up, bootstrap-heating, and depletion of the DT fuel, its expansive disassembly, and thermonuclear ignition by propagating burn from central hot-spots in the microspheres are discussed. Extensive numerical results from a 3-T Lagrangian simulation code are presented. The yields Y_o from uniform 10, 1, and 0.1μg microspheres with densities ρ = 1 to 4×10^4 g/cm^3 and temperatures $T_e = T_i$ = 1.8 to 100 keV are given. It is shown that $Y_o \sim \rho^{2/3}$ for spheres of fixed mass m. The gain-factor $G_o \equiv Y_o/mI_o$ (I_o is the internal energy) is shown to measure burn efficiency in uniform microspheres. More than a four-fold increment in the gain factor is shown to derive from apportionment of the internal energy in a central hot-spot. The limiting effects of electron degeneracy on the gain factor are outlined. As a guideline, the experimental observation of 10^{13} neutrons/kJ of input laser energy is established as proof of good absorption; 10^{15}/kJ will imply yields exceeding break even.

I. INTRODUCTION

Computer simulations[1] indicate that a laser driven ablative implosion scheme[2] may suffice to compress the inner regions of small DT spheres and shells to extreme densities and temperatures, such that net thermonuclear energy is produced prior to the expansive disassembly of these targets. Details of the thermonuclear burn in DT microspheres at high density therefore become of interest. From a comprehensive understanding of the burn phenomenology, it should be possible to designate the conditions which the implosion scheme must establish for efficient burn of the DT fuel, and the degree to which it is permissible to deviate from these conditions. With this motivation, in this paper, we present results from extensive simulation studies of the burn-up and disassembly of microspheres for a broad range of masses, initial densities and temperatures. We emphasize the effects of localized bootstrap-heating, and propagating burn from central hot-spots.

Similarity solutions[3,4] and numerical treatments[5] for the disassembly of laser irradiated targets have been available in the literature for some time. However, these papers ignore thermonuclear burn. Recently, Johnson and Hall[6] have calculated the yield from expanding solid density pellets. Their similarity treatment applies if both bootstrap-heating and fuel depletion are negligible during the burn.

Calculations for our high density study were performed with the one-dimensional Lagrangian hydrodynamics code used for Ref. 1. It allows for separate ion, electron, and radiation temperatures (a Planckian spectrum for the radiation is assumed). The code employs classical conductivities[7] for the electrons and ions, and classical coupling rates between the electron and ion temperature fields. It accounts for Compton and inverse-Compton scattering, and bremsstrahlung and inverse-bremsstrahlung between the electrons and the radiation field. It calculates

the energy released from D-T and competing D-D nuclear reactions, accounting for time-dependent, nonlocal α-particle energy deposition into the electrons and ions. The computations utilize tabular, Fermi-Thomas Dirac equations of state, including the effects of electron Fermi-degeneracy on the pressure, internal energy and opacity of the equimolar DT fuel. Auxiliary calculations were carried out with a separate nonequilibrium Lagrangian code that does Monte-Carlo radiation and reaction product particle transport, to provide a cross-check on our results. We report good agreement between the two sets of calculations.

The utility of high compression for enhancing the rate of energy release in systems undergoing nuclear reactions was recognized at Los Alamos as early as 1943.[1] Its use in laser fusion had to await the development of powerful short-pulse lasers, as are now under construction at Los Alamos and Livermore. Reference 1 provided a quantitative picture of the performance anticipated from DT targets exposed to highly optimized laser pulses. Here we look more closely at the interactive hydrodynamics and thermonuclear chemistry that follow from high compression. In Sec. II, we justify the choice of initial conditions inspected. Section III outlines the pertinent aspects of burn physics, introducing the concept of spherical propagating burn-waves. Section IV collects and summarizes the results of more than 800 numerical simulation runs (each requiring, typically, 30 min of CDC 6600 CPU time). Finally, Sec. V relates our results to the predictions of Ref. 1. Also, it establishes guidelines -- estimates of likely neutron production from laser irradiated targets -- which should help to gauge the success of early laboratory experiments.

II. INITIAL CONDITIONS

Our choice of initial conditions was guided by the optimized implosion results of Ref. 1. There it was suggested that a laser input energy of 0.7kJ/μg of DT was required for good yields, and that, typically, the final compressed pellet core represented ∿10% of the original pellet mass. Thus, 2kJ were required for a 3μg pellet, of which the inner ∿0.3μgs were brought to burn conditions. Consequently, we have studied the burn in 10μg, 1μg, and 0.1μg microspheres, corresponding to laser inputs of 65kJ, 6.5kJ, and 650J, respectively. The latter energies are consistent with the 10kJ per nanosecond-pulse lasers anticipated for the near future.[8]

In the Ref. 1 3μg pellet implosion, a core density above $10^4 g/cm^3$ was calculated. The present simulations, therefore, went to $4\times10^4 g/cm^3$. In solid density DT, the energy gain from nuclear reactions exceeds the bremsstrahlung loss[9] when the electrons and ions are above 4keV temperatures -- provided that the α-particle reaction products are recaptured by the plasma; so our runs were made at 3keV and higher. At $\rho R > 1$ (for example, $\rho > 3000$ g/cm^3 in the 1μg microsphere), it was found that inverse bremsstrahlung lowered the ignition requirements, so a few calculations were made down to 1.8keV. In the optimized implosion scheme, high temperatures in the pellet cores were first achieved hydrodynamically by the collapse of overtaking, coalescing shocks just outside the center. This process produces, typically, 10 to 15keV central temperatures, which subsequently initiate the thermonuclear burn. Thus 20keV was the maximum initial temperature chosen for most of our runs, although a few were made with temperatures as high as 100keV to observe the consequences of the drop-off in the DT reaction cross-section[10] $\langle\sigma v\rangle$ beyond $T_i = 65$keV. Generally, we started with the electron and ion temperatures equal, i.e., $T_e = T_i \equiv T$, and with the initial radiation temperature T_r at 1 keV. For simplicity, we restricted our propagation study to burn initiated by 10keV hot-spots in a 1 keV ambient background.

III. PHENOMENOLOGY

A. Burn-up

DT burn is characterized by the reaction time $\tau_r = 1/(n\,\sigma v)$. The fuel is comsumed in accordance with the burn-up equation[11]

$$\frac{df_r}{dt} = (1 - f_r)^2 \frac{1}{2\tau_r} \quad , \tag{1}$$

in which $f_r \equiv (n_\alpha + n_n)/n_D + n_T + n_\alpha + n_n)$, or equivalently, $f_r \equiv Y/326\ m)$, Y being the yield in kJs and m being the pellet mass in μgs. Equation (1) describes the progress of the reaction D + T → n + α, in which the neutron is given 14MeV and the α-particle 3.5MeV. With a constant τ_r, Eq. (1) has the solution

$$f_r(t) = \frac{t/2\tau_r}{1+t/2\tau_r} \sim \begin{cases} t/2\tau_r, & t << 2\tau_r \quad (2a) \\ 1 - \dfrac{2\tau_r}{t}, & t >> 2\tau_r \quad (2b) \end{cases}$$

At large times, $t >> 2\tau_r$, the fuel is strongly depleted, being mostly burned to α's and neutrons. From Eq. (2b), we see that the asymptotic rate of burn-up goes as $(\tau_r/t)^2$.

Bootstrap heating occurs when temperatures in the burning regions of a pellet are raised by redeposition of the α-particle reaction energy. In our simulations, the energy of the α particles generated in the DT fusion reaction is deposited along their path length by Coulomb collisions (see Longmire[12]). The range energy relationship is approximately

$$\frac{dU}{dx} = -23.2\left(\frac{\rho}{\rho_o}\right)\frac{U^{1/2}}{T_e^{3/2}}\left\{1 + 0.17\ \ln\left[T_e\left(\frac{\rho_o}{\rho}\right)\right]\right\}^{1/2} - 0.047\left(\frac{\rho}{\rho_o}\right)\frac{1}{U}\left\{1 + 0.075\ \ln\left[T_e^{1/2}\left(\frac{\rho_o}{\rho}\right)^{1/2} U^{1/2}\right]\right\} \quad (3a)$$

where T_e, the electron temperature, is in keV, $U \equiv E_\alpha/3.5\text{MeV}$ (E_α is the α energy), and ρ_o is the solid DT density, 0.213 gm/cm^3. The first term represents the energy deposited in electrons; the second represents energy deposited in DT ions. From Eq. (3a), it it can be seen that when $U = 1$ and T_e is a few tens of kilovolts, the electron term dominates. However, as U decreases along a trajectory, the ion term eventually dominates. In fact, for these lower values of T_e, exact integrations show the energy deposition rate falling gradually along a trajectory and then rising sharply near the end. Useful estimates of the α range under different conditions can be obtained by integrating Eq. (3a) first with just the electron term, neglecting the ion term, and then with just the ion term. The resulting ranges are, respectively, in centimeters,

$$\lambda_{\alpha e} = AT_e^{3/2}/\rho,\ A = 0.086\rho_o\left\{1+0.17\ \ln\left[T_e\left(\frac{\rho_o}{\rho}\right)^{1/2}\right]\right\}^{-1} \quad (3b)$$

and

$$\lambda_{\alpha i} = B/\rho,\ B = 10.65\rho_o\left\{1+0.075\ \ln\left[T_e^{1/2}\left(\frac{\rho_o}{\rho}\right)^{1/2}\right]\right\}^{-1}. \quad (3c)$$

The coefficients A and B are relatively slowly varying function of ρ and T_e. The correct range, which is less than either Eq. (3b) or (3c), is approximately given by Eq. (3b) at small T_e and by (3c) at large T_e. In all of these estimates, we have assumed that the α velocity is less than the electron thermal velocity, which requires that $T_e > 1$ keV. Also, U was set equal to one in Eq. (3c). It should be noted that when the ion term is strong, there is also significant scattering of the α particles, so that the range calculated from Eq. (3a) is only an upper limit on the distance between the point of origin of an α and the end point of its trajectory.

An expression equivalent to Eq. (3a) has been integrated numerically, giving the results plotted in Fig. 1a. For this integration, separate terms were used for the energy deposition into the deuterons and tritons, and the $\ln(U^{1/2})$ term was approximated by $[\ln(1) + \ln(T_e^{1/2})]/2 = 0.5\ \ln(T_e^{1/2})$. When U dropped to T_e, the remaining α energy was given to the ions. We find that a good fit to the computed range results for $\rho = .213$ g/cm^3 is

$$\rho\lambda_\alpha = \frac{1.5\times10^{-2}T_e^{5/4}}{1 + 8.2\times10^{-3}T_e^{5/4}}\ (\text{g/cm}^2) \quad (3d)$$

(accurate to ~2% for T_e from 1 to 100keV). Above

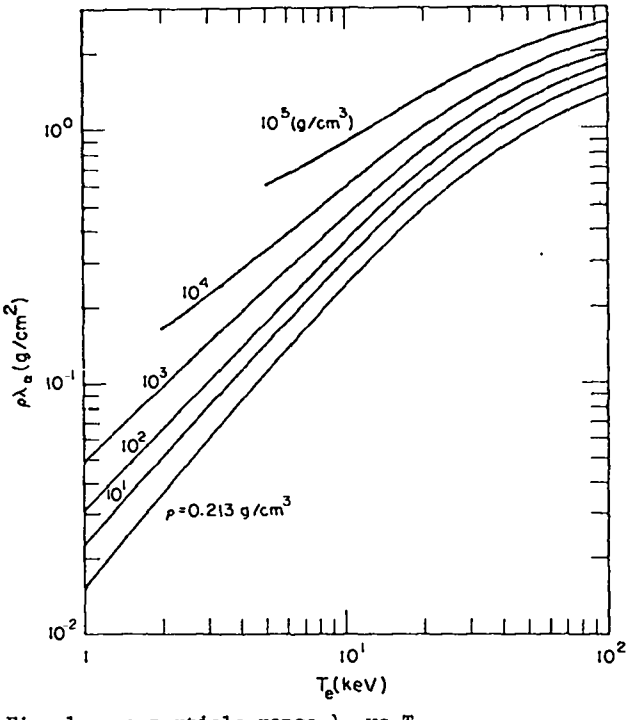

Fig. 1a. α particle range λ_α vs T_e.

10keV, as ρ goes from solid density to 10^4 g/cm^3, the range is increased by roughly a factor $\delta(\rho) = 1 \rightarrow 3$ by the Coulomb logarithmic terms. Thus, in proportion to the radius R of a microsphere

$$\frac{\lambda_\alpha}{R} \approx \frac{1.9\delta(\rho)}{[1 + 122/T_e^{5/4}]} \Big/ \rho R. \qquad (3e)$$

As T_e rises, an increasingly larger fraction f_i of the total α energy is absorbed by the ions. The temperature at which the ions and electrons absorb equal fractions is $T_e = 32$keV at solid density, for which the simple rule

$$f_i = \frac{1}{1 + 32/T_e} \qquad (4)$$

agrees with the Fig. 1b results from integration to 2% for $T_e > 6$keV. With increased ρ, the logarithmic terms reduce the equipartition temperature so that at 10^4 g/cm^3, $f_i = 0.5$ at only $T_e = 24$keV.

In the simulations with our equilibrium code, non-local, time dependent α-particle energy transport was carried out using Eq. (3a), in an S_n treatment,[13] employing 6 (and 12) energy groups, with n = 2 in most cases (and n = 4 in a few to test accuracy). In the non-equilibrium code, used as a cross check, the transport was accomplished by a Monte Carlo scheme, accounting for the Eq. (3a) energy loss to Coulomb drag.

In uniformly burning spheres, the centers capture the energy preferentially. The edges encounter α's only from the interior; the center "sees" an isotropic source distribution. Figure 2 describes the burn-up of a sphere which has its boundary

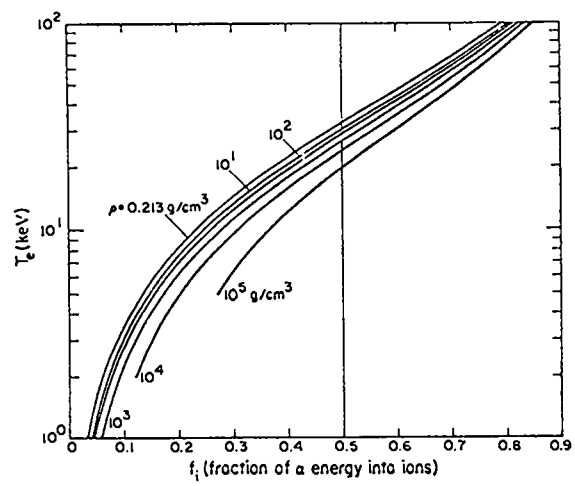

Fig. 1b. α energy absorption.

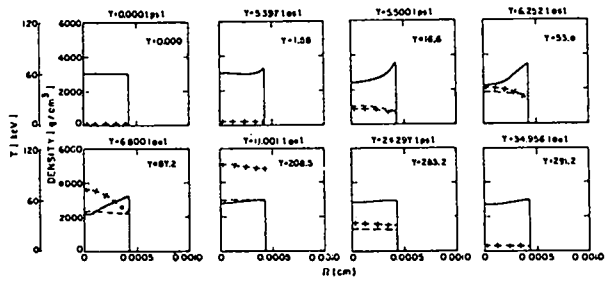

Fig. 2. Burn-up of a 1μg sphere with a fixed outer boundary; ρ = 3000 g/cm , T = 3keV. T_i +++, T_e --- . Evident bootstrap-heating.

artificially fixed; i.e., an infinite confinement time applies. Initially, T = 3keV, m = 1μg, ρ = 3000 g/cm^3, and thus ρR = 1.28. Note that ρR vs ρ plots are provided in Fig. 3; also, from Fig. 1a [or Eq. (3e), $\lambda_\alpha/R = 0.13$, so effective α recapture should be evident. The relative mean-free-path for photons[7] (at the average photon energy) is

$$\lambda_p/R \approx \frac{1.3\ T_e^{7/2}(\text{keV})}{\rho} \Big/ \rho R = 1.7\times10^{-2} \qquad (5)$$

so inverse-bremsstrahlung retards the photon loss from the microsphere, T_e remains up, and the fuel ignites at 3keV. at first, t < 5 psec, electron heating is favored. But by t = 6.252 psec, $T_e > 32$keV at the center. Then T_i can surpass T_e and rise to over 100keV. The preferential central heating and the need for pressure balance produce a significant depression of density in the middle of the microsphere during the first 10 psec. Thereafter, fuel depletion, in accordance with Eq. (1) (for an appropriate mean τ_r), significantly reduces the energy production rate. The ion thermal energy couples into the electrons, and then into the radiation

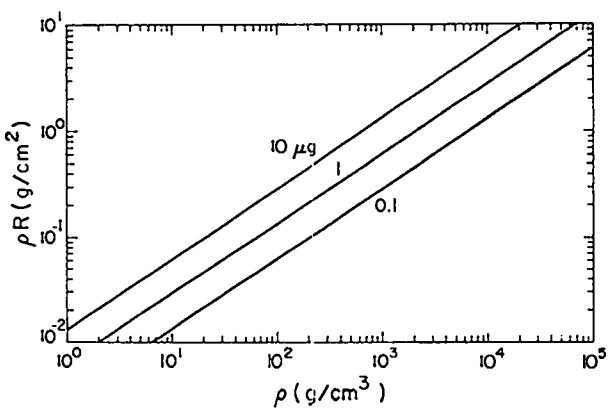

Fig. 3. ρR vs ρ for spheres of 10, 1, and 0.1μgs.

field. After 35 psec, the burn is quenched, since the net energy loss through radiation exceeds the depleted production rate. Of the 326kJ ideally available from the DT microgram, only 291kJ are released.

B. Disassembly

In the case of a free boundary, the first expansion wave signaling disassembly reaches the center of the sphere in a time R/C_s, where $C_s = [(\gamma_i P_i + \gamma_e P_e)/\rho]^{\frac{1}{2}}$ is the speed of sound. Generally, $\gamma_i = \gamma_e = 5/3$. But in some cases, the high electron conductivity can make the electrons isothermal, i.e., effectively $\gamma_e = 1$. Alternatively, bootstrap-heating can make $P_i >> P_e$, and heightened ion conductivity can produce the tendency $\gamma_i \to 1$. Thus, at high temperatures, in the extreme, $C_s \to (P_i/\rho)^{\frac{1}{2}} = (T_i/m_i)^{\frac{1}{2}} = V_{th}$, but most often $C_s \to \sqrt{10/3}\, V_{th}$.

As temperature is decreased, on the other hand, there is a minimum pressure

$$P_e = nT_{ef}\left[1 + \frac{\pi^2}{15}\left(T_e/T_{ef}\right)^2 + \cdots\right] \ (\mathrm{keV/cm^3}) \quad (6)$$

consistent with the Fermi-degeneracy of the electrons. As usual, $\epsilon_f = h^2/2m_e\,(3/8\,n_e)^{2/3}$, while here we have defined an "equivalent Fermi temperature" $T_{ef} \equiv 2/5\ \epsilon_f$, such that $3/2\ T_{ef} = 3/5\ \epsilon_f$ -- the mean kinetic energy of electrons in the limit of full degeneracy[14] ($T_e \to 0$). For DT,

$$T_{ef}\ (\mathrm{keV}) = 5.65\times10^{-3}\,\rho^{2/3}\ (\mathrm{g/cm^3}) \ ; \quad (7)$$

T_{ef} is 2eV at solid density, and 0.94keV at $10^4 \times$ solid. For T_e near T_{ef}, the degeneracy "floor" on P_e must force more rapid disassembly than anticipated classically. At $\rho = 10^4$ g/cm^3, for example, $T_{ef} = 3.6$keV so that at $T_e = 1$ keV, Eq. (6) gives a pressure $\sim$2.9 times greater than the usual $P_e = n_e T_e$.

The outer half-radius of a sphere contains 88% of its mass and, on the average, only half the mass in a given ΔR is burning while the expansion wave is crossing. These effects reduce the effective disassembly time to $\tau_e = R/4C_s$. That is, for a sphere, the mean burning mass to time $t = R/C_s$ is

$$\langle m(t)\rangle = \frac{\int_0^{t=R/C_s} \frac{4\pi\rho}{3}\left(R - C_s t\right)^3 dt}{R/C_s} = \frac{m(t=0)}{4},$$

and, since $\tau_e\ m(t=0) \equiv \langle m(t)\rangle R/C_s$, $\tau_e = R/4C_s$.

We define f_{ro} and Y_o as the fractional burn-up encountered and the yield produced in the full disassembly of initially uniformly heated microspheres. We can use τ_e in Eq. (2a) to predict f_{ro} and Y_o, provided the initial density and temperature are low enough so that there is only negligible fuel depletion and bootstrap heating. Thus, for $\tau_e << 2\tau_r$, we get

$$f_{ro} = \frac{\tau_e}{2\tau_r} = \left(\frac{\langle\sigma v\rangle}{8C_s m_i}\right)\rho R, \quad (8a)$$

and

$$Y_o = D\rho R\ , \quad D = \frac{326m\langle\sigma v\rangle}{8C_s m_i}\ , \quad (8b)$$

so that for a family of microspheres of fixed mass m and different initial densities

$$Y_o = E\rho^{2/3}\ , \quad E = \left(\frac{3m}{4\pi}\right)^{1/3} D\ . \quad (8c)$$

Figure 4 shows the burning of the Fig. 1 1μg sphere when its outer boundary is free. There is minimal bootstrap heating, T has risen from 3 to 4 keV by 3 psec, and by 6 psec most of the yield (only .7kJ) is out. By this same time, the infinitely confined system had heated to 40keV, with a large reduction in T_r, and with 50kJ released. Figure 5 shows how the yield improves in the free system when we start at 20keV. The long interval for bootstrapping is avoided, so that by 2.1 psec, we have the Fig. 2 energy output to 3.3 psec. By 3.4 psec, however, expansion has terminated the burn. Note that in Fig. 5, T_i first exceeds T_e at $t = .83$ psec when the central $T_e = 40$keV, in agreement with Eq. (4). Note also that the flat T_e profiles in the low density exterior of the pellet derive from the high electron thermal conductivity operating there.

C. Energy Gain

At high density ($\rho R > 1.0$), the microspheres

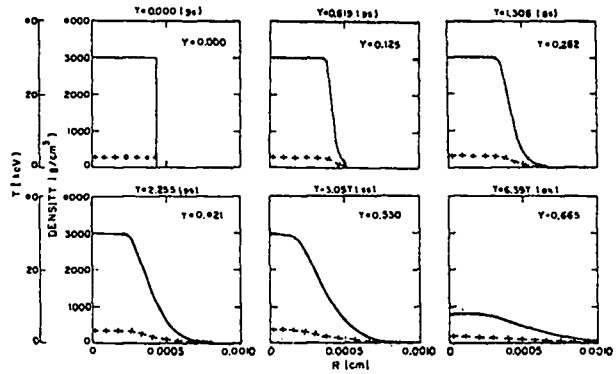

Fig. 4. Burn-up and disassembly of the Fig. 2 sphere, free outer boundary.

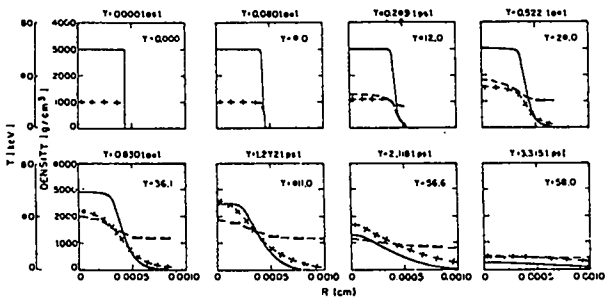

Fig. 5. The Fig. 3 sphere with $T_i = T_e = 20$keV initially.

will ignite at 3keV by virtue of inverse-bremsstrahlung, as demonstrated by Figs. 2 and 4. But at 10 - 20keV, the yield is significantly improved by circumventing the bootstrap-heating time. Going higher in temperature is not helpful, since between 20 and 70keV the yields are nearly constant with only a slight peak at 40keV, the $(\langle\sigma v\rangle/C_s)$ maximum. In any case, high temperatures require greater laser input energy. At nondegenerate densities, DT has the specific internal energy

$$I = I_i + I_e$$
$$= 5.8\times10^{-2}(T_i(\text{keV}) + T_e\ (\text{keV}))\ (\text{kJ}/\mu\text{g}) \quad . \qquad (9)$$

In practice, we will want to optimize the gain-factor

$$G_F = \frac{Y}{mI} \quad . \qquad (10a)$$

For uniformly heated systems, G_F becomes

$$G_o = \frac{Y_o/m}{I_o} \quad . \qquad (10b)$$

At fixed ρ and m (or ρR), optimization selects a temperature that provides the best specific yield for the specific internal energy invested in the microsphere. The mass of the microsphere can then be adjusted to match mI_o to the energy delivered to the core of the pellet in laser-pellet interaction experiments. At small ρR, where Eq. (8) applies, the optimum T is near 12keV (borne out by our simulations), since $\langle\sigma v\rangle/C_s$ declines at larger T while I_o rises, and since Y_o drops as $\sim T_i^3$, dominating over the decrease in I_o as we go to lower T. With large ρR ($\geq$1.0, from the simulations), on the other hand, the optimum T declines, since bootstrap-heating can raise the microsphere to a good burn temperature, even though less I_o is invested. In the limit, as ρR is increased, the optimum T approaches the ignition temperature, which itself is dropping from its solid density value (4keV), as a consequence of heightened inverse-bremsstrahlung.

D. Central Ignition and Propagating Burn

A further and significant improvement in the gain factor can be made, if I is apportioned so that just a central region of the microspheres is heated to ignition temperature, under conditions that spherical thermonuclear burn-wave then propagates out, igniting the rest of the fuel. Such burn-wave propagation was first openly discussed in Ref. 15. Its favorable influence was implicity included in the Ref. 1 results, however, where propagation progressively improves the yield with increasing pellet mass. Discussions of plane burn-wave propagation in solid density DT are available in the literature.[11,16,17]

Figure 6 depicts propagating burn in a 10μg microsphere. The sphere is initially uniform at $\rho = 6\times10^3$ g/cm^3, so ρR = 4.4. A vertical line demarks the inner 10% of the mass; it is at 20keV; the remaining outer mass is at 1 keV. At first, the electrons bootstrap-heat in the inner region, and conduct into the outer one. At the same time, the outer mass is compressed somewhat by the expanding inner fuel. The capture of α's from the center, ion conduction, and electron-ion exchange have brought $\sim$40% of the outer ions to 20keV by 1.2 psec. The outer region is then burning to high depletion. It reimplodes the center between 2 and 2.4 psec. Then finally, by 5.4 psec, the burn has been quenched by disassembly. The yield is 1.245×10^3 kJ. When this same sphere is started at a uniform, 20keV temperature, it burns to $f_r = .42$, yielding 1.369×10^3 kJ. So with central ignition we release 91% of the yield of the uniform case by investing only 18% of its energy -- for a 5.2-fold multiplication in the gain-factor.

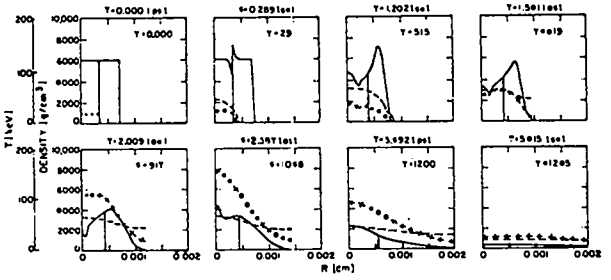

Fig. 6. Propagating burn in a 10μg sphere; free outer boundary. Inner 10% of the mass T = 20keV; remaining mass T = 1 keV.

From this example we conclude that it is useful to define a multiplication factor M_c, characterizing the gain from central ignition, such that

$$G_F = G_o M_c \quad , \quad M_c \equiv \frac{Y}{Y_o} \frac{I_o}{I} \quad . \tag{11}$$

Then G_o is the gain from a uniformly heated microsphere at temperature T, internal energy I_o, and yielding Y_o, while Y is the yield from the same microsphere with a central hot-spot at T, and a cooler exterior, so that a lower specific internal energy I is implied. In the Fig. 6 example, $Y/Y_o = 0.91$, $I_o/I = 5.7$, and $M_c = 5.2$

The multiplication from central ignition would be slightly higher, i.e., $M_c \sim 6.3$, were it not for electron degeneracy. At $\rho = 6\times10^3$ g/cm^3, $T_{ef} = 1.87$keV. At 1 keV, the cold region in Fig. 6 is therefore degenerate with a specific internal energy

$$I_c = 5.8\times10^{-2}\left\{T_i(\text{keV}) + T_{ef}(\text{keV})\left[1 + \frac{\pi^2}{15}\left(\frac{T_e}{T_{ef}}\right)^2 + \cdots\right]\right\} \text{ (kJ/}\mu\text{g)} \quad , \tag{12}$$

[following Eq. (6)] that is, 1.7 times its classical value, reducing M_c only marginally, since most of the energy still resides in the central 20keV region.

In general, for spheres with such hot-spots, we can write

$$\frac{I_o}{I} = \frac{mI_o}{m_h I_o + (m - m_h)I_c} = \frac{1}{f_h + (1 - f_h)\frac{I_c}{I_o}} \quad , \tag{13}$$

in which $f_h = m_h/m$ is the fraction of the pellet mass that is hot. For effective central ignition: (a) first, the full pellet must have a large enough ρR so that, if it were uniformly hot, there would be overall α-particle recapture and bootstrap-heating, leading to a good fractional burn-up ($f_{ro} \gtrsim 0.2$) and a correspondingly high Y_o; (b) then, for an optimal M_c, the hot fraction f_h must be small -- but not too small, since for $Y/Y_o \sim 1$, the radius of the hot region must exceed λ_α for its initial burn to be sustained by bootstrap heating, while propagation ignites the neighboring cold region. These conditions imply a high density in microspheres ($\gtrsim 10^4$ solid), so degeneracy will place a significant floor on I_c/I_o. In our Fig. 6 for example, $f_h \sim I_c/I_o \sim 0.1$.

A central hot spot is provided by the final shock collapse in optimized implosions,[1] so $M_c > 1$ can be anticipated. Also, the shock energy dumps primarily into the ions, which can increase G_F by effecting a higher early burn rate. Finally, since burn begins with the shock collapse, this moment can serve as t = 0 for the studies which follow.

IV. NUMERICAL RESULTS

A. Y_o

Figures 7a-d show the computed yields from uniform microspheres with various initial ρ and T.

At low densities (<100 g/cm^3 for each of the three masses, 10, 1.0, and 0.1μg), the $Y_o \sim \rho^{2/3}$, in agreement with Eq. (8c). In fact, estimates from Eq. (8) are quite accurate. With 10μg, for example, when $\rho = 10$ g/cm^3 and T = 3keV, we get $\rho R = 6.2\times10^{-2}$ g/cm^2 and $\tau_e/\tau_r = 1.15\times10^{-4}$ [see Fig. 8 in which the ordinate τ_e/τ_r is simply $(\langle\sigma v\rangle/4C_s m_i)\rho R$ from Eq. (8a)], so $f_{ro} = 5.8\times10^{-5}$ by Eq. (8), and $Y = 326(10)f_r = 1.9\times10^{-1}$ kJ, which lies on the appropriate Fig. 7a curve. As density is increased, bootstrap-heating eventually raises the computed yields above the Eq. (8) predictions; this occurs for $\rho > 700$ g/cm^3 in the 10μg pellet. Finally, with still further ρ increases, the yield curves flatten out from fuel depletion. As we go from 10 to 0.1μg, the densities characterizing the onset of depletion are 10^3, 3×10^3, and 10^4, corresponding to the yields 600kJ, 60kJ and 6kJ, respectively.

We considered that our code's prediction of ignition for high density DT at 3keV might sensitively depend on its use of a radiation diffusion treatment. Consequently, our 10μg results were checked by a separate series of calculations with an independent, non-equilibrium code that does frequency dependent Monte Carlo radiation transport (and also Monte Carlo α-particle transport). Its results are the x-sign data in Fig. 7a. Generally, the two sets of results are in good agreement. However, the Monte Carlo calculations show no descent below a $Y_o \sim \rho^{2/3}$ dependence in the $100 < \rho < 700$ g/cm^3 range like the dip predicted by the diffusion treatment. Also, the x-data bootstraps at slightly lower ρ.

Figure 7d more clearly shows the T dependence of Y_o in 10μg spheres. The peak yields are near 40keV. But the dependence becomes increasingly flatter as we go to higher density, so that at 3000 g/cm^3, Y_o in nearly constant between 10 and 70keV.

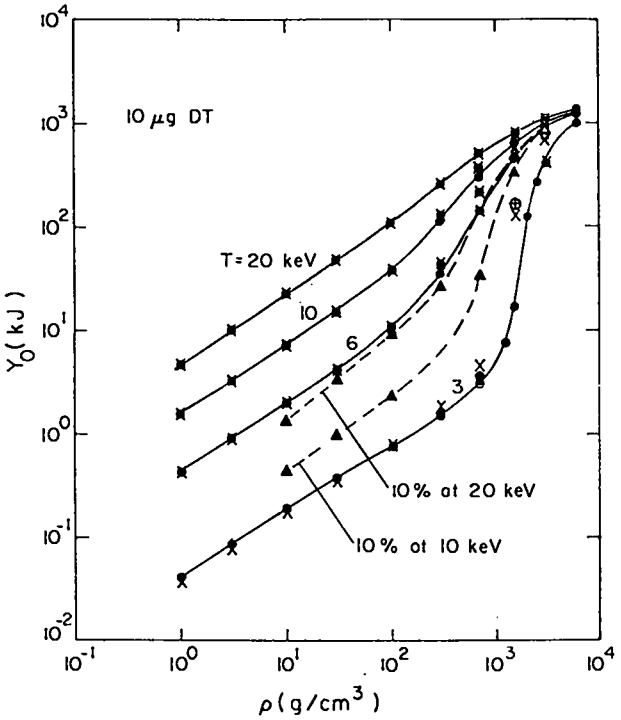

Fig. 7a

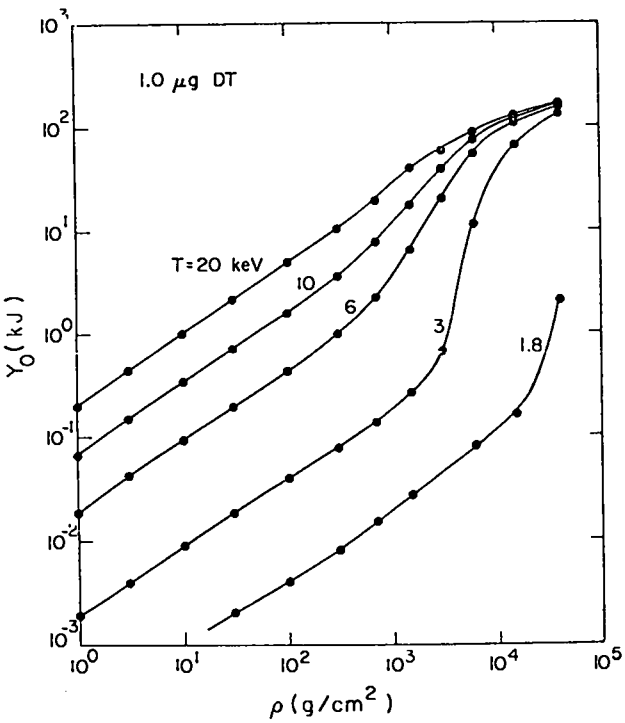

Fig. 7b

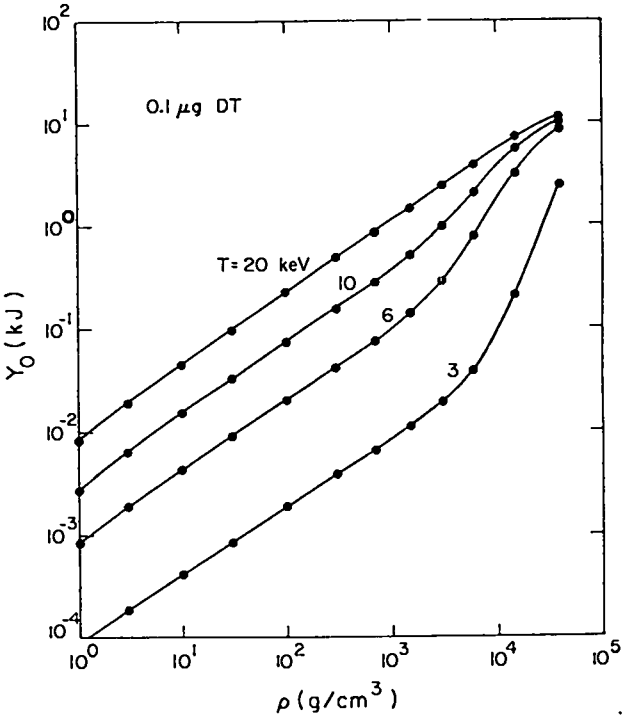

Fig. 7c

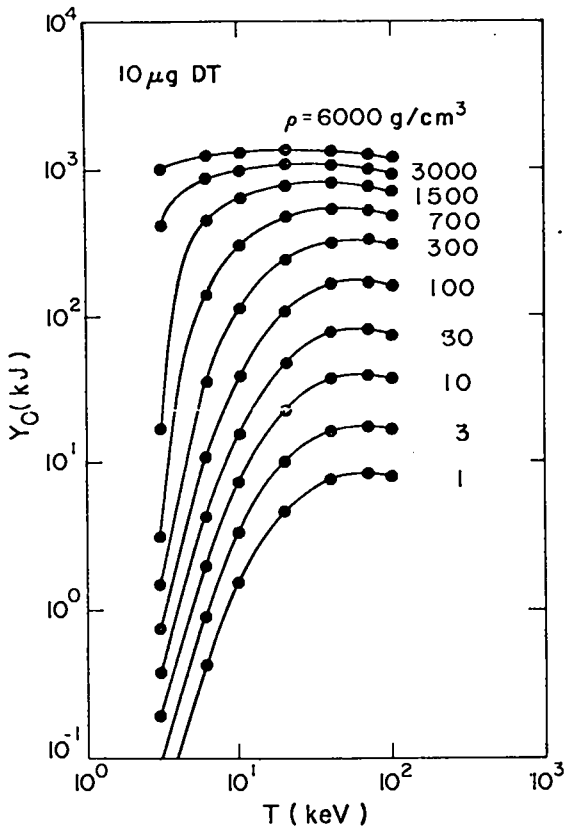

Fig. 7d

Fig. 7. Y_o vs ρ in spheres of: a/ 10μg, b/ 1μg, and c/ 0.1μg. The dashed curves in a are for just the inner 10% of the mass at 10 and 20keV. The x-data was recalculated with an independent non-equilibrium code. The ⊕ data includes neutron energy redeposition for T = 3keV. d/ Details the temperature dependence in the 10μg sphere.

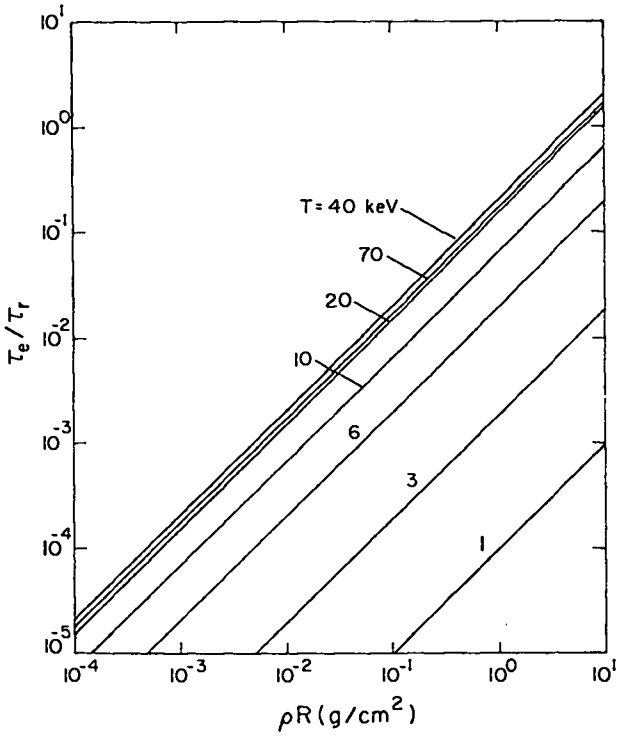

Fig. 8. τ_e/τ_r vs ρR.

On Fig. 7a, we have included the yields obtained when only the inner 10% of the 10μg pellet is at 10 and 20keV, while its outer mass starts at 1 keV. Clearly, these yields have the same general ρ dependence (inclusing net bootstrapping above 700 g/cm^3) as the curves for uniformly heated microspheres. At 100 g/cm^3, λ_α is too large for either bootstrapping or effective propagation. Consistently, from the Fig. 7a data with Eqs. (11) and (13) (and accounting for degeneracy in the cold region), we calculate M_c = 0.23 and 0.47 with the hot-spot at 10 and 20keV, respectively. At 10^4 g/cm^3, on the other hand, the yields are essentially the same as with uniform heating, so $M_c \to I_o/I \sim 3.9$, and 5.7 for the two temperatures. Still it should be recognized that even at densities where propagation fails, it is advantageous to apportion the internal energy in a central hot-spot, since this can increase the yield by establishing a higher average burn rate. With the 10keV hot-spots, for example, the average pellet temperature is 2.5keV, but the yields roughly equal those from 4keV pellets until ρ > 1000 g/cm^3, when the situation further improves because propagation becomes significant.

B. $f_r(t)$

Figure 9 shows the time dependence of the burn-up fraction $f_r(t)$ in 1μg pellets at 3000 g/cm^3. The results are for both a fixed and free outer boundary; they include the Fig. 2, 4, and 5 runs. The temperatures are 3, 6, and 20keV for which the reaction times $\tau_r(T_i)$ = 710, 51, and 3.3 psec, respectively.

With a fixed boundary and T = 3 (compare Fig. 2), $f_r(t)$ undergoes linear growth to 0.5 psec and then bootstrap heating thereafter. The heating is strongest ($f_r \sim t^{7.5}$) from 4 to 6 psec. Depletion slows the burn rate for f_r > 0.3. The T = 6 result is similar, but with the strong bootstrapping coming in sooner -- from 1 to 3 psec. With T = 20, there is nearly linear burn to 2 psec followed by depletion.

With the free boundary, 90% of Y_o is out in each of the three cases by $t = R/2C_s$ [$R/C_s(T_i)$ = 6.9, 4.8, and 2.7 psec]. Thus, we see that the effective burn time is <u>not</u> $\tau_e = R/4C_s$ [Eq. (8)], as at lower densities, since all three cases are bootstrapping. At T = 3 keV, the unbootstrapped final $f_r \equiv f_{ro}$ [extrapolating the Fig. 7b curve] would be 1.1×10^{-3}, while the observed f_{ro} is 2×10^{-3}. The T = 6 case disassembles, while still in the strong bootstrap phase. In fact, its effective burn time (based on T ≡ 6keV) exceeds R/C_s. Depletion is unimportant in these three cases since they disassemble leaving f_{ro} < 0.2.

C. f_{ro} and G_o vs ρR

When Y_o is converted to f_{ro} and the Fig. 7a-c data is plotted vs ρR, it collapses to one curve for each of the temperatures studied with the mass dependence explicitly removed -- except for $\rho R \gtrsim 2.0$, where degeneracy effects noticeably reduce f_{ro} at small m and T [see Fig. 10a].

From Eq. (8), this scaling was anticipated for $\rho R < 0.2$ g/cm^2, for which there is little bootstrap-heating. But it also works for larger ρR, because λ_α/R [Eq. (3e)] also scales with ρR. Equation (3e) indicates that at 10keV and $10^3 \lesssim \rho \lesssim 10^4$ g/cm^3, for example, α's from the center of the microsphere have $\lambda_\alpha < R$ for $\rho R \gtrsim 0.73$. Clearly, the degree of bootstrap-heating depends on the fraction of α's f_α recaptured in the pellet. In Fig. 10b, we plot the f_α's calculated in our various runs. Good scaling with ρR is evident, but the larger masses recapture α's somewhat more effectively (2-6%) at all ρR.

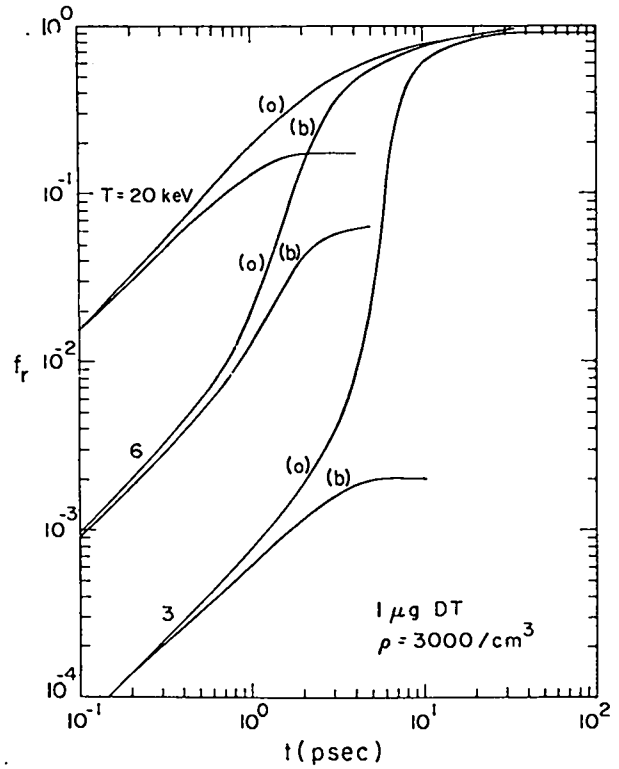

Fig. 9. Time dependence of the burn fraction $f_r(t)$ in 3, 10, and 20keV, 1μg spheres with a/ fixed boundaries, and b/ free outer boundaries.

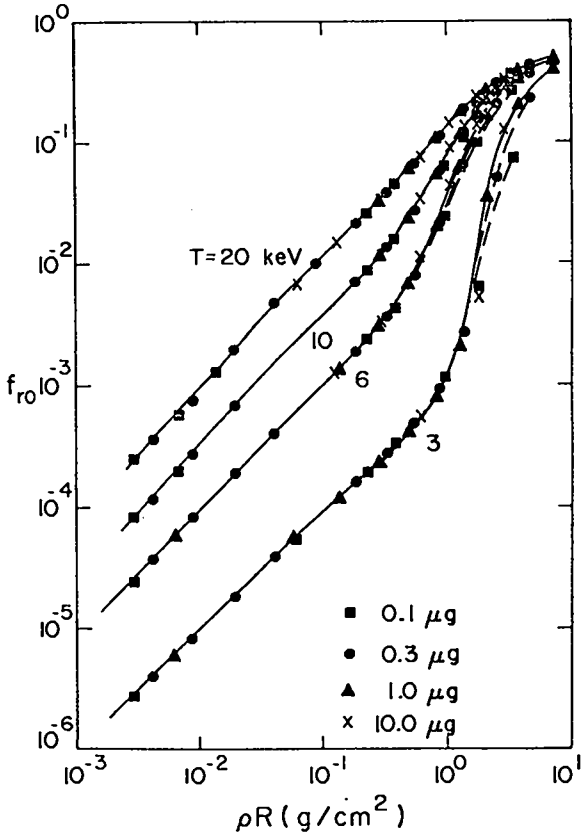

Fig. 10a

This is consistent with a greater energy absorption rate from an increase in the log terms in Eq. (3b), as we go to the smaller ρ corresponding to larger m at fixed ρR. With different masses $m = 4\pi/3\ \rho R^3$, this correspondence is, of course,

$$\rho \sim \frac{(\rho R)^{3/2}}{m^{1/2}} \sim \text{const}\ m^{-1/2} \quad . \tag{14}$$

By now it should be evident that it is extremely difficult to burn more than 30% of the fuel. Above $f_r = 0.3$, depletion begins to severely reduce the effective burn rate, requiring increasingly longer inertial confinement times. At 20keV and $\rho R \geq 1.28$, the effective burn time is $\tau_b = R/2.4C_s$ (see Fig. 9),=due to the bootstrap-heating. The use of $t = \tau_b$ in Eq. (2) and the conversion $\tau_b/\tau_r = 1.7(\tau_e/\tau_r) \sim 0.32\rho R$ (on the average between 20 and 70 keV -- see Fig. 8) -- gives

$$f_{ro} = \frac{\rho R}{6.3 + \rho R} \quad , \quad \begin{matrix} \rho R \gtrsim 1 \\ 20 < T < 70\text{keV} \end{matrix} \quad , \tag{15}$$

which predicts $f_{ro} = 0.41$ at $\rho R = 4.4$, for example, in agreement with the Fig. 10a results.

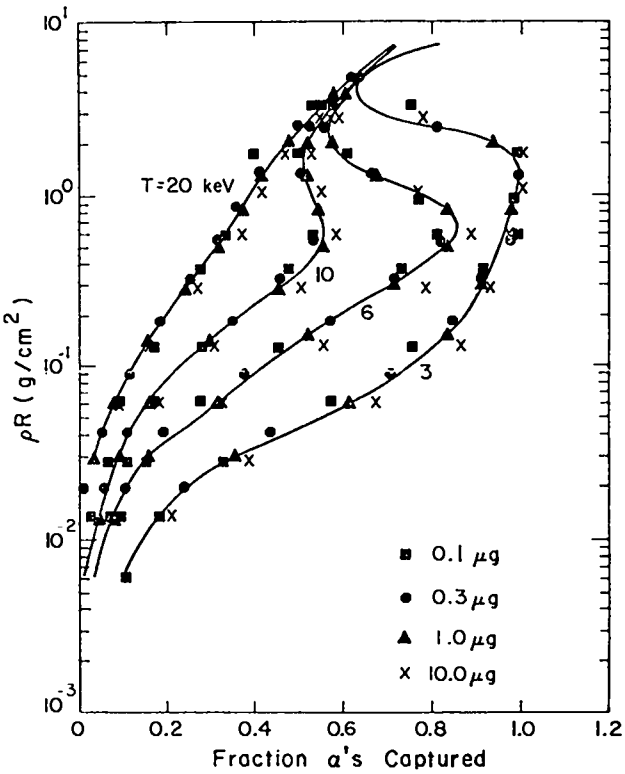

Fig. 10b

We must remember, however, that the 14meV neutrons have a 22 cm mean-free-path[18] in solid density DT. In analogy, therefore, with Eq. (3e),

$$\frac{\lambda_n}{R} = 4.6/\rho R \quad . \tag{16}$$

So for $\rho R \gtrsim 4.6$ and $f_{ro} \gtrsim 0.42$, neutron energy is recaptured, complicating the phenomenology. Neutron recapture effects are discussed in Section V.

The gain-factor G_o also scales well with ρR. The Fig. 10c curve is a composite constructed from an overlay of all our run results. It applies for $\rho < 6000$ g/cm^3. Above this density, degeneracy effects begin to seriously split each T curve, giving lower gains as m decreases. We see that G_o exceeds unity at 20keV for $\rho R > 0.1$. For $\rho R \sim 1$, the T curves cross, and the bootstrap-heating permits us to achieve higher gain-factors by starting at lower initial temperatures. Figure 10d is derived from 10c and gives the iso-gain-factor contours for uniformly heated microspheres with $\rho < 6000$ g/cm^3. It shows that for each ρR there is an optimal I_o giving the best G_o. At $\rho R = 2.15$ (10^4 × solid density with 10μgs), the best G_o (≈80) comes for I_o = 0.8kJ/μg. The dashed line through the minimal I_o values give the phenomenological rules: $I_{o|min} \sim (\rho R)^{-0.8}$, $G_{o|max} \sim (\rho R)^{1.58}$, $0.56 \lesssim \rho R \lesssim 2.45$. Note that if the effects of depletion can be circumvented, so that all the fuel is burned, then starting it at the classical ignition temperature,[9] $T_i = T_e$ = 4keV, gives a theoretical maximum G_o = 699.

D. M_c

To get a quantitative understanding of the possible advantages from central ignition, we conducted a series of runs for microspheres of different ρR and m, in which an inner fraction of the mass f_h was started hot at 10keV, while the remaining fraction was set at 1 keV (as for Fig. 6). When $f_h = 1$, it follows that $Y = Y_o$, $M_c = 1$ [see Eq. (11)] and $G_F = G_o$. In each series of runs, f_h was decreased until $M_c \ll 1$.

Figure 11a shows that for $\rho R \gtrsim 2$, the ratio Y/Y_o declines gradually until f_h reaches some threshold value, after which Y drops away extremely rapidly. From the intersections of asymptotes drawn tangent to the flat portions of the 10μg curves, we have determined that at the drop-off $f_h = f_{h|min}$ = 0.1, 0.015, and 0.002 for ρR = 1.35, 2.15, and 3.90

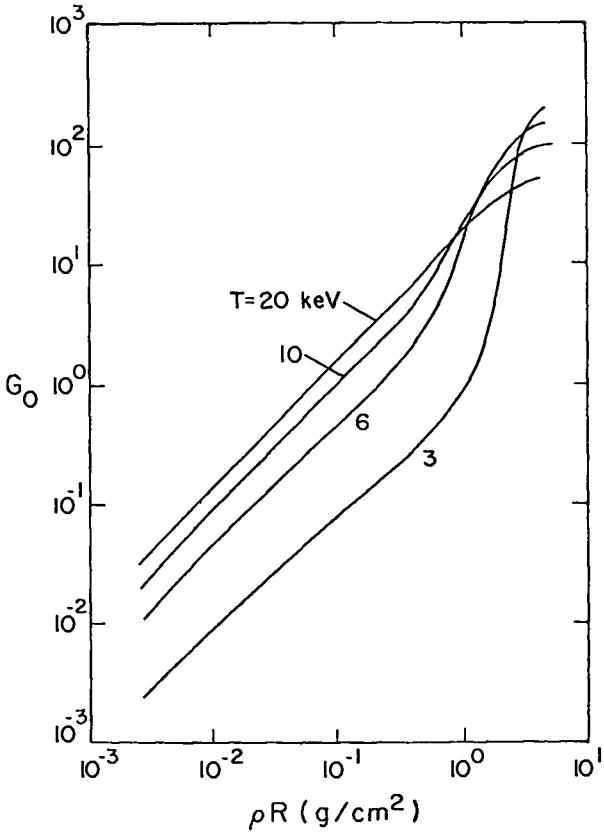

Fig. 10c

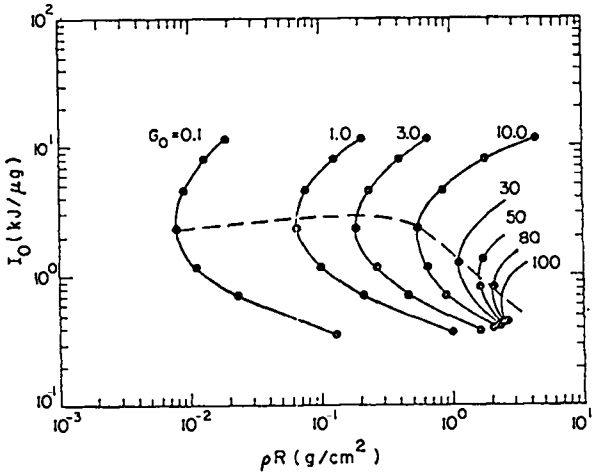

Fig. 10d

Fig. 10. ρR dependence of: a/ the burn-up fraction f_{rq}, b/ the fraction of α's recaptured f_α, and c/ the gain-factor G_o for uniformly heated spheres, d/ iso-gain factor contours vs I_o and ρR.

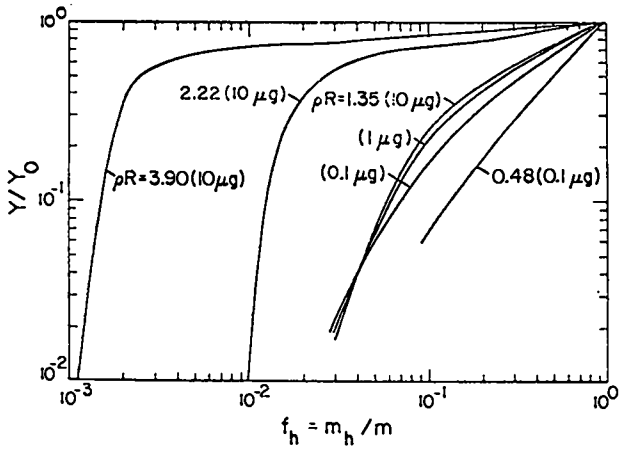

Fig. 11a

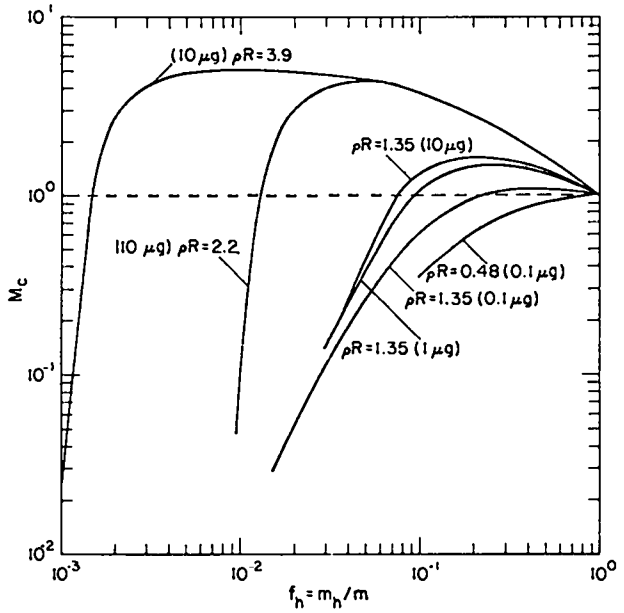

Fig. 11b

Fig. 11 Dependence on the fraction of mass hot f_h with central ignition of: a/ the scaled yield Y/Y_o, and b/ the central ignition multiplier M_c.

respectively. Since $f_h \equiv m_h/m = (\rho R_h)^3/(\rho R)^3$, these results imply $f_{h|min} = (0.5)/(\rho R)^3$ and thus $\rho R_{h|min} = 0.8$. But with this ρR_h (at 16keV and with $10^3 \lesssim \rho \lesssim 10^4$ g/cm^3) $\lambda_\alpha/R_h = 1$. Assuming, then, that bootstrap heating provides a 16keV environment, on the average, we conclude that λ_α serves as a minimum radius for hot-spots inaugurating successful propagation. Clearly, propagation must fail in the $\rho R = 0.48$ (0.1μg) spheres, since for them $f_{h|min} = 0.5/(0.48)^3 = 4.0$, i.e., $\lambda_\alpha >> R$. The gradual decline in Y/Y_o for $f_{h|min} << f_h \lesssim 1$ derives from the additional time, relative to the uniform case, required for propagated ignition of the fuel.

Since, generally, $Y/Y_o < 1$ with central ignition, gain multiplication must come from a reduction in the required internal energy. From Eq. (13), the maximum $I_o/I \to I_o/I_c$, $f_h << 1$. At $\rho = 2130$ g/cm^3, for example, $I_o/I_c = 9.5$ (it is not 10 because of degeneracy -- see the equation of state data in Fig. 12). The multiplications M_c computed for various f_h are plotted in Fig. 11b. The competing effects of decreased I, and decreased Y give a maximum $M_c^* = 4.1$ at $\rho R = 2.2$ in the 10μg pellet. The unfavorable influence of degeneracy is evident in the $\rho R = 1.35$ results which show M_c^* dropping from 1.5 to 1.05, as m changes from 10 to 0.1μgs. From the M peaks in Fig. 11b, we have determined the phenomenological rule, $m^*(g) = 4.9\times10^{-2}\ \rho^{-3/2}$, for the optimal pellet mass at each density examined. With it, we conclude that the best choice for f_h is

$$f_h^* = \frac{3(4.9\times10^{-2})\ \rho^{-3/2}}{4\pi\ \rho R^3} = 1.2\times10^{-2}\ \rho^{\frac{1}{2}}/(\rho R)^3 \ . \qquad (17)$$

For example, $f_h^* = 0.05 = 3f_{h|min}$ for $\rho = 2130$ g/cm^3 and $\rho R = 2.2$ in the 10μg pellet.

V. FINAL CONSIDERATIONS

In laboratory laser-pellet interaction experiments, the yield ratio $Y_R = Y/E_L$ is of consequence; E_L is the energy absorbed from the laser. Also of importance is the coupling efficiency $\varepsilon = mI/E_L$ between the absorbed E_L and the internal energy mI of the microsphere core of the pellet;

$$Y_R \equiv Y/E_L = \frac{\varepsilon Y}{mI} = \varepsilon G_F = \varepsilon G_o M_c \ . \qquad (18)$$

In this paper, we have examined the dependence of G_o and M_c on various possible initial states of the fuel. A general connection between Y_R and E_L cannot be drawn, however, in the absence of more precise information on the core conditions established by the laser-driver hydrodynamics, as implicitly determined in the Ref. 1 calculations.

Still, to relate the present work to our earlier results for laser-imploded pellets, we give the following example: Let $\varepsilon = 0.1$. Suppose the laser compresses the 10μg core of the larger pellet to 10^4 × solid density, so its $\rho R = 2.2$. Imagine that a final shock collapse leaves the optimal mass fraction

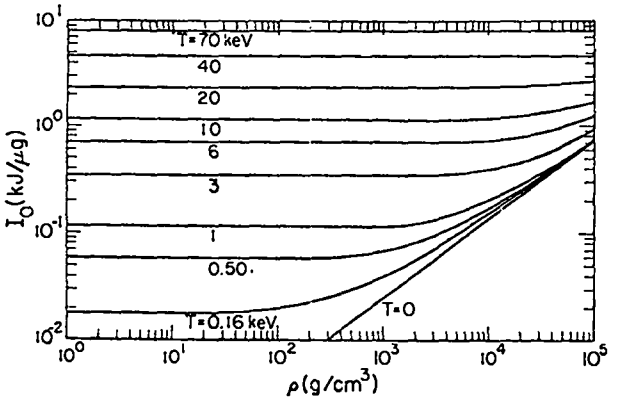

Fig. 12. I_o vs ρ in equimolar DT for $T_e = T_i \equiv T$, $T_r^o = 0$; note the asymptotic approach to the degeneracy floor on I_o for $T < 10$ and $\rho \to 10^5$ g/cm³.

at 10keV and the background at 1 keV. Then $f_h^* = 0.05$ and $M_c^* = 4.1$ [Fig. 11b]. The uniform gain-factor $G_o = 62$ at 10keV and this ρR [Fig. 10c]. So, Eq. (17) predicts $Y_R = 0.1(62)4.1 = 25.4$. At 10keV, $I_o = 1.22$kJ/μg, while $I_o/I = 6.0$, when $f_h = f_h^*$. This means that 0.20kJ/μg is needed, for a total of 2kJ over the whole 10μg microsphere. In accordance with the value of ε, it follows that $E_L = 20$kJ. This yield ratio and input energy agree with the Ref. 1, Fig. 2e optimized results for shells. The yield is $Y = Y_R/E_L = 508$kJ. It represents the burn-up of 10μgs to $f_{ro} = 0.16$. At 10keV, Fig. 10a predicts $f_{ro} \simeq 0.22$; multiplication by the correction $Y/Y_o = 0.7$ [Fig. 11a] for central ignition also gives $f_{ro} = 0.16$. Finally, to complete the picture, we recall that Ref. 1 recommended $E_L = 0.7$kJ/μg, based on the full pellet mass M for optimized yields. This sets M at 28.6μgs. So, in fact, the microsphere-core is roughly 35% of the mass.

A few additional comments should be made about our high density results. (a) First, recall that the neutron mean-free-path, Eq. (15), falls within the microspheres, $\lambda_n < R$, for $\rho R \lesssim 4.6$. Therefore, at $\rho R = 2.2$, for example, some fractional recapture of the neutrons occurs, and, on the average, 4meV is transferred to the DT per interaction (reduced from 14meV by the mass differential). Consequently, we made a small sub-group of runs, including S_n neutron transport. These have shown, for example, that neutron recapture lowers the density threshold for 3keV ignition in the 10μg microsphere, giving 100kJ yields at only $\rho = 1000$ g/cm³ [the ⊕ data point in Fig. 7a] -- instead of at 1500 g/cm³, as computed with α-recapture alone. (b) Then, note the following disclaimer to our results involving degeneracy at high density. Although the thermodynamics has been corrected for degeneracy, e.g., the internal energy in the 1 keV outer regions of the pellets of our propagation study [Section III.D], we use classical transport coefficients and classical mean-free-paths to determine the energy flow. The inclusion of degeneracy in the electron thermal conductivity and in the cross-section for α particles against degenerate electrons, as examples, could significantly modify the efficiency of central ignition.

Early laser-initiated DT burn experiments will most readily involve unignited burn -- the $Y_o \sim \rho^{2/3}$ regime. The practical achievement of extreme DT densities serves as a special challenge. The neutrons produced experimentally are a useful diagnostic; 3.6×10^{14} are created per kilojoule of thermonuclear energy yield, or roughly 10^{17} neutrons are available from the complete consumption of 1μg of DT. Figure 13 shows the iso-neutron contours, derived principally from the Fig. 10a burn-up data for disassembling spheres. It gives the neutrons produced per microgram of DT versus the specific internal energy of the fuel and its ρR. The ρR of 1μg of DT at solid density is 2.2×10^{-3}. From Fig. 13 we conclude that with 1 kJ uniformly deposited in the 1μg, $\sim 6\times10^{12}$ neutrons can be released at solid density. The important point to be made here is that, although such a neutron release is impressive by conventional Controlled Thermonuclear Reaction standards, it is in no way proof of large compressions, and represents an output energy that is 60-fold short of breakeven.

We see that as experiments begin with the new 1 to 10kJ laser systems, the production of 10^{13} neutrons/kJ of laser input can serve as a bench-mark, implying effective absorption, and presumably, some compression, compensating for the laser energy lost to blow-off. Progress toward a breakeven demonstration can then be measured by how close we come to the production of 10^{15} neutrons/kJ, as the technology advances.

ACKNOWLEDGMENTS

Numerous co-workers at Los Alamos Scientific Laboratory have aided us in the course of this work.

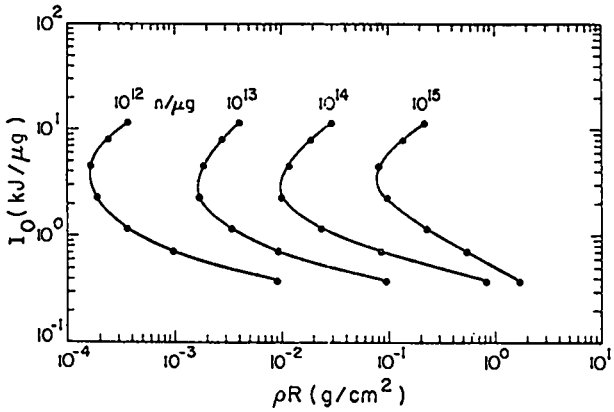

Fig. 13. Iso-neutron output contours vs I_o and ρR.

We are grateful to H.N. Fisher for critical discussions, to Dr. G.F. Evans for providing the data on α particle ranges and deposition, and to Dr. G.I. Kerley, J. Rood, and Dr. J. Barnes for the DT equation of state data at degenerate densities.

APPENDIX A

The use of solid DT pellets in laser-interaction experiments presents certain technical difficulties, principally in the area of cryogenics. These may be avoided, at least in early investigations, by the use of LiDT targets. To examine the ramifications of this possibility, the thermonuclear-burn characteristics of LiDT spheres have been calculated. Figures 14a-c give our results for the burn-up fraction f_{ro}, gain G_o, and gain multiplication M_c of Li^6DT microspheres of mass m = 10μg.

This compound has a mean atomic number $\overline{Z} = 2$, $\overline{Z^2} = 5$, and a mean atomic mass number $\overline{A} = 4.25$ -- compared to $\overline{Z} = 1$ and $\overline{A} = 2.5$ for pure DT. In LiDT, the number fraction of deuterons is $f_D = 0.5$ -- one deuteron for every two LiDT's; in pure DT, $f_D = 1.0$. The thermonuclear yield from the complete burn-up of this fuel, i.e., $f_{ro} \to 1$, by the D-T reaction is 95.9 kJ/μg.

By arguments similar to those accompanying Eq. (8a), we find that for Li^6DT spheres

$$f_{ro}|_{LiDT} = f_D \left(\frac{\overline{A}_{DT}}{\overline{A}_{Li^6DT}} \right)^{\frac{1}{2}} f_{ro}|_{DT} = 0.383\, f_{ro}|_{DT}\,, \tag{A-1}$$

in the absence of significant bremsstrahlung loss, bootstrap-heating, and fuel depletion. The Li^7DT isotope gives ~5% less burn-up, since its $\overline{A} = 4.75$. The Fig. 14a results agree with this [Eq. (A-1)] behavior in the $\rho R < 3\times10^{-2}$ regime with T = 3, and for $\rho R < 8\times10^{-2}$ for $T \geq 6$.

The rate of bremsstrahlung loss per unit mass in each fuel has the dependence

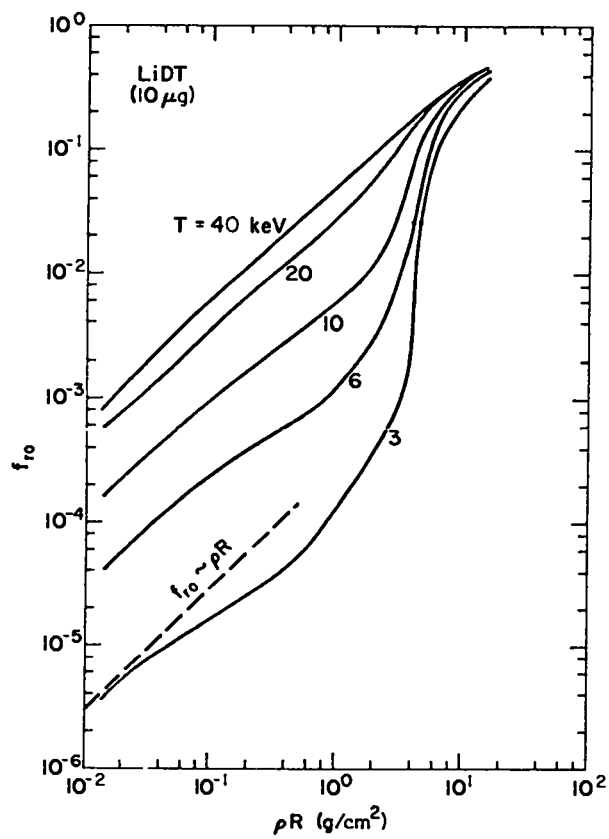

Fig. 14a

$$\partial I/\partial t|_b \sim \left(\frac{\overline{Z^2}}{\overline{A}} \right) \frac{Z}{T_e^{\frac{1}{2}}}\,,$$

while the rate of thermonuclear energy generation from the D-T reactions obeys

$$\partial I/\partial t\big|_r \sim \left(f_D/\bar{A}\right)^2 \langle\overline{\sigma v}\rangle .$$

The specific bremsstrahlung rate is 3.46 times higher in LiDT: the specific energy production rate is 11.6 times lower. In the range T = 3 to 10keV, $\langle\overline{\sigma v}\rangle \sim T^{3.5}$, so to compensate for the increased loss from bremsstrahlung, T must be increased by a factor of 3.4. Thus, while the ignition temperature is 4keV in DT, in LiDT it rises to 13.7keV. This value applies assuming $T_e = T_i$ equilibrium, negligible inverse-bremsstrahlung, and redeposition of the 3.5 meV α particle reaction products alone. With complete neutron energy redeposition as well, i.e., a total of 17meV redeposited per reaction, the LiDT ignition temperature drops to 8.1keV. Finally, with increased inverse-bremsstrahlung at large ρR, giving a short photon mean free path [as in Eq. (5)], the ignition temperature falls below 3keV, as evident from the $f_{ro}|_{LiDT} = 0.3$ calculated for ρR = 15 and T = 3keV. At this temperature, one sees increased f_{ro} from α redeposition for $0.5 \lesssim \rho R \lesssim 2.2$, and a further, more pronounced, increase from the neutron energy redeposition for ρR > 2.2. The total scattering cross-section for 14meV neutrons[18] is ∿0.9 barns off DT, and ∿1.5 barns off Li^6. This gives a neutron mean-free-path of 3.5cm in solid density Li^6DT, so that in comparison to the radius R of a microsphere

$$\frac{\lambda_n}{R}\Big|_{LiDT} \approx \frac{3.0}{\rho R} \quad . \qquad (A\text{-}2)$$

This is consistent with the strong f_{ro} rise for ρR > 2.2. The cross sections increase with lower neutron energies. Thus, following the first scatter, subsequent events become more probable, aiding the energy redeposition. The three temperature code was used in all the LiDT simulations; its S_n neutronics treatment accounts for the total energy deposition from these multiple scatterings. Additional energy (and Tritium) can be generated by the reaction

$$n + Li^6 \rightarrow \alpha + T + 4.17meV .$$

At 14meV, however, the cross section for this reaction is only 0.026 barns (∿93 times lower than the net scattering cross section), so the yield it adds is small. Still the effects of this reaction are included in the Fig. 14 results.

For large ρR and T = 20 to 40keV

$$f_{ro}|_{LiDT} \quad \frac{\rho R}{18.3 + \rho R} \approx 0.45 \text{ when } \rho R = 15. \qquad (A\text{-}3)$$

This can be compared with the Eq. (15) result for DT. Again, roughly a three-fold increase in ρR is needed before the LiDT burn-up fraction approaches that of DT.

The specific internal energy of fully ionized Li^6DT, taken as a perfect gas, is

$$I\big|_{LiDT} = \frac{3}{2}\,\frac{k(T_i + \bar{Z}\,T_e)}{\bar{A}m_A}$$

$$= 3.41\times10^{-2}\ [T_i(keV) + 2T_e(keV)]\ kJ/\mu g \quad , (A\text{-}4)$$

where m_A is the atomic mass unit 1.66×10^{-24} gm. This is 88% of the specific internal energy of pure DT for $T_e = T_i$ [see Eq. (9)]. The specific yield from our uniform LiDT spheres is $Y_o/m = 95.9\ f_{ro}|_{LiDT}$ kJ/μg. Burn performance is measured by the gain factor

$$G_o|_{LiDT} \equiv \frac{Y_o}{mI} = \frac{95.9\ f_{ro}|_{LiDT}}{1(kJ/\mu g)} \quad . \qquad (A\text{-}5)$$

Figure 14b shows that the gain at 6keV exceeds the 20keV gain for $\rho R \gtrsim 5.0$; in DT, this cross-over occurs for $\rho R \approx 1$. Depletion limits the 6keV LiDT gain to $G_o(\rho R > 15) \rightarrow 58$; the corresponding limit in DT is $G_o(\rho R > 4) \rightarrow 180$.

Figure 14c gives the results of the Sec. III D. M_c calculation for LiDT. An inner fraction f_h of the initial pellet mass was started at 10keV; the remaining outer mass was at 1 keV. We see that at ρR = 6.2, for example, central ignition provides an $M_c \gtrsim 2$ [see Eq. (11)] with only ∿6% of mass heated to 10keV. The comparable DT figure is $M_c(\rho R \gtrsim 2.2) = 4$.

The optimally imploded DT spheres of Ref. 1 achieved a peak ρR near 1.9. Our most recent, refined calculation with the Ref. 1 code employing non-local α energy deposition predicts a $Y_R \gtrsim 25$ [see Eq. (18)] from a 7.5μg sphere, absorbing 5.3 kJ of 1.06μ laser light. Moreover, these calculations predict that an LiDT sphere of the same mass will compress to ρR = 6.3, giving a peak $Y_R = 1.5$, under the same time-tailored pulse, run until 26 kJ has been deposited in the pellet.

Under adiabatic compression, $I \sim \rho^{2/3} \sim \rho R$. The input energy required for central ignition should, in general, vary as $E_{IN} \sim I/M_c$. Thus, we may anticipate that

$$E_{IN}|_{LiDT} \Big/ E_{IN}|_{DT} = \left(\frac{\rho R}{M_c|_{LiDT}}\right)\Bigg/\left(\frac{\rho R}{M_c|_{DT}}\right) = \left(\frac{6.3}{2}\right)\Bigg/\left(\frac{1.9}{4}\right) \gtrsim 6 \qquad (A\text{-}6)$$

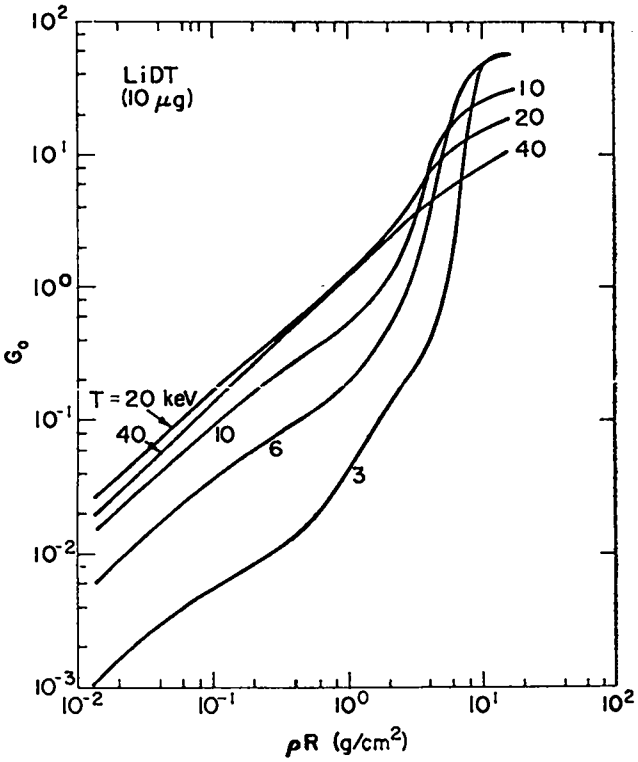

Fig. 14b

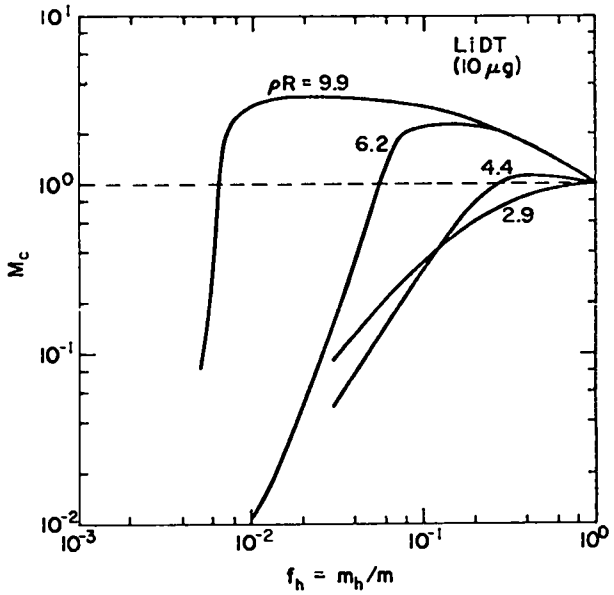

Fig. 14c

Fig. 14. ρR dependence in Li^6DT of: a/ the fractional burn-up f_{ro}, b/ the gain factor G_o, and c/ the multiplication from central ignition with different mass fractions f_h at 10keV.

is required in optimal implosions, as we have calculated. Finally, since under comparable conditions, the gain factors $G_o|_{DT}$ $G_o|_{LiDT}$ = 2.7, we see that the calculated seventeen-fold reduction in Y_R for optimally imploded LiDT spheres is consistent with our Fig. 14 results.

APPENDIX B

I. THREE TEMPERATURE CODE

Our one-dimensional, three temperature, Lagrangian code has, in spherical geometry, the equations of motion

$$\frac{\partial u}{\partial t} = -\frac{1}{\rho}\frac{\partial}{\partial r}(P+q) = -r^2\frac{\partial}{\partial m}(P+q) \qquad \text{(B-1)}$$

in which $m = \int_o^r \rho r^2\, dr$ is the mass/steradian, $\rho = 1/v$ with v the specific volume, and $\partial r/\partial t = u$. P is the sum of the three fluid pressures, i.e., $P \equiv P_e + P_i + P_r$, and q is the Von-Neuman artificial viscosity.

The coupled energy equations are

$$\frac{\partial T_i}{\partial t} = \frac{1}{C_{vi}}\left[\dot{S}_i - \left(P_i + q + \frac{\partial I_i}{\partial v}\right)\frac{\partial v}{\partial t} - A_{ie}(T_i - T_e) + \frac{v}{r^2}\frac{\partial}{\partial r}\left(r^2 K_i \frac{\partial T_i}{\partial r}\right)\right] \qquad \text{(B-2a)}$$

$$\frac{\partial T_e}{\partial t} = \frac{1}{C_{ve}}\left[\dot{S}_e - \left(P_e + \frac{\partial I_e}{\partial v}\right)\frac{\partial v}{\partial t} - A_{er}(T_e - T_r) + A_{ie}(T_i - T_e) + \frac{v}{r^2}\frac{\partial}{\partial r}\left(r^2 K_e \frac{\partial T_e}{\partial r}\right)\right], \qquad \text{(B-2b)}$$

$$\frac{\partial T_r}{\partial t} = \frac{1}{C_{vr}}\left[-\left(P_r + \frac{\partial I_r}{\partial v}\right)\frac{\partial v}{\partial t} + A_{er}(T_e - T_r) + \frac{v}{r^2}\frac{\partial}{\partial r}\left(r^2 K_r \frac{\partial T_r}{\partial r}\right)\right]. \qquad \text{(B-2c)}$$

Each equation is derived using the chain rule

$$\frac{\partial I}{\partial t} = C_v\frac{\partial T}{\partial t} + \frac{\partial I}{\partial v}\frac{\partial v}{\partial t}, \quad \text{where } C_v \equiv \frac{\partial I}{\partial T}.$$

If the ions and electrons were perfect gases, then relations

$$P_i = \rho I_i, \quad I_i = 3/2\ kT_i/m_i, \quad C_{vi} = 3/2k/m_i$$
$$P_e = \rho I_e, \quad I_e = 3/2\ kT_e/m_i, \quad C_{ve} = 3/2\ k/m_i \tag{B-3}$$

would apply. In fact, there is a vast spectrum of real material effects, including: phase changes, dissociation, ionization, pressure ionization, and degeneracy, which alter the Eqs. (B-3) so that, for our calculations, their equivalents are obtained from carefully compiled equations-of-state tables, as are the derivatives $\partial I_{i,e}/\partial v$.

The radiation diffusion treatment was included to examine changes in ignition temperature from the increased opacities at high density. The use of Eq. (B-2c) assumes that the photons achieve Planckian equilibrium, characterized by a radiation temperature T_r, at a rate much faster than their equilibration rate with local electrons, or the rates characterizing the changes of other significant parameters in each burn sequence. The radiation is, thus, characterized by a pressure, specific internal energy, and specific heat,

$$P_r = \rho I_r, \quad I_r = \frac{4\sigma}{c\rho} T_r^4, \text{ and } C_{vr} = \frac{4I_r}{T_r} .$$

The fields are coupled by the coefficients $A_{ei} = C_{vi}\ \nu_{eq}$

$$\nu_{eq} = \frac{8(2\pi)^{1/2} m_e^{1/2} e^4 N_A^2}{3} \left(\frac{Z^2}{A^2}\right) \ln \Lambda_{ei} \frac{\rho}{(kT_e)^{3/2}} \left[1 - \frac{3}{2}\frac{T_i}{T_e}\frac{m_e}{m_i}\right] , \tag{B-4a}$$

$$K_i = 20\left(\frac{2}{\pi}\right)^{3/2} \frac{(kT_e)^{5/2}\ k}{m_i^{1/2}\ e^4 Z^4\ \ln\Lambda_i} , \tag{B-4b}$$

$$K_e = 20\left(\frac{2}{\pi}\right)^{3/2} \frac{(kT_e)^{5/2}\ k\varepsilon\delta_T}{m_e^{1/2}\ e^4 Z\ \ln\Lambda_{ei}} , \tag{B-4c}$$

from Spitzer,[7] in which

$$\varepsilon\delta_T = \frac{0.43Z}{(3.44 + Z + 0.26\ \ln[Z])}$$

and

$$\ln\Lambda_{ei} = \max\left\{1,\ \ln\left[\frac{3}{2e^3}\left(\frac{A}{Z}\frac{k^3 T_e^3}{\pi N_A \rho}\right)^{1/2} \frac{1}{\left(Z + \frac{1}{2\alpha c}\sqrt{\frac{3kT_e}{m_e}}\right)}\right]\right\} , \tag{B-5a}$$

$$\ln\Lambda_i = \max\left\{1,\ \ln\left[\frac{3}{2e^3 Z^2}\left(\frac{A}{Z}\frac{k^3 T_i^3}{\pi N_A \rho}\right)^{1/2} \frac{1}{\left(Z + T_i/T_e\right)^{1/2}}\right]\right\} . \tag{B-5b}$$

In these expressions, N_A is Avagadro's number. The ratio Z/A is 0.4 and 0.47 for fully ionized DT and LiDT, respectively. With partial ionization, we use an "effective Z" from the equation of state tables. Also, k is the Boltzmann constant and $\alpha = e^2/\hbar c$, the fine structure constant. The factors $\varepsilon\delta_T$ provide thermo-electric and electron-electron collision corrections to the electron conductivity. The argument Λ_{ei} is the harmonic mean of the classical and quantum results.[7] In addition,

$$A_{er} = C_{ve}\ (\nu_b + \nu_c) ,$$

$$\nu_b = \frac{32}{3}\left(\frac{2}{\pi m_e}\right)^{1/2} \frac{e^4 N_A^2}{\hbar c}\ k\left(\frac{Z^2}{A^2}\right) \frac{\rho Z}{(kT_e)^{1/2}}\ G(T_r/T_e) \tag{B-6a}$$

with

$$G(\gamma) = \int_0^\infty \frac{d\xi f(\xi)\left[1 - e^{-\xi(\frac{1}{\gamma} - 1)}\right]}{(\gamma - 1)\left(1 - e^{-\xi/\gamma}\right)} , \tag{B-6b}$$

containing

$$f(\xi) = \int_1^\infty \ln\left(\sqrt{x} + \sqrt{x+1}\right) e^{-\xi x}\ dx ,$$

the bremsstrahlung emission spectrum. A simplified fit to $G(\gamma)$ is used in the calculations; for $\gamma \equiv T_r/T_e \to 0$, $G(\gamma) \to 1$, making ν_b the pure bremsstrahlung rate; for $\gamma \to \infty$, $G(\gamma) \to \pi^2/4$, giving pure inverse-bremsstrahlung. Also,

$$\nu_c = \frac{128}{3}\frac{\pi e^2 \sigma}{(m_e c^2)^2}\ N_A\left(\frac{Z}{A}\right) T_r^4\ k \tag{B-6c}$$

is the Compton scattering rate in our radiation diffusion model; here σ is the Stephan-Boltzmann constant. Equations (B-6a-c) are due to Hurwitz.[19] Finally, we note that the radiative conductivity

$$K_r = \frac{16\sigma\ \lambda_R}{3} T_r^3 = \frac{16\sigma}{3\rho K_R} T_r^3 \quad , \qquad \text{(B-7)}$$

in which λ_R, the Rosseland mean-free-path, has the λ_p dependence of Eq. (5), when inverse-bremsstrahlung dominates. In the calculations K_R, the Rosseland mean opacity, is obtained from tables, calculated to include the effects of bound-free transitions, bremsstrahlung and collision absorption, Compton scattering, and line absorption.

The competing thermonuclear reaction rates obey

$$\frac{\partial N_D}{\partial t} = - N_D^2 \ (\overline{\sigma v})_{DD} - N_D N_T (\overline{\sigma v})_{DT}$$

$$\frac{\partial N_T}{\partial t} = - N_D N_T (\overline{\sigma v})_{DT} + 0.25\ N_D^2 (\overline{\sigma v})_{DD} \quad . \qquad \text{(B-8)}$$

Analytic fits to Tuck's[10] Maxwell averaged cross-sections, $(\overline{\sigma v})$, were used for the computations. In general, the DD reactions contributed less than 1% of the energy release in our runs. For the appended LiDT results, the energy released and absorbed in n-Li reactions was also calculated.

The α particles and neutrons are transported in accordance with the Boltzmann equation, solved by the S_n method of Carlson,[13] with n typically 2 for α's and 4 for neutrons. Details of the α particle energy deposition scheme are given in Sec. III a. The energy fron neutron scattering is given to the background ions. In n-Li reactions, the energy exchange is local by a prescription similar to Eq. (4). The deposited energy enters the ion and electron fields through the $\dot{S}_{i,e}$ specific energy source rate terms in Eqs. (B-2a-c).

In differencing the hydrodynamics and energy equations, typically 40 to 100 zones were used with r and u assigned to the zone boundaries (j), and intensive properties, e.g., ρ and T, assigned to zone centers (j+½). The artificial viscosity used is

$$q_{j+\frac{1}{2}} = \begin{cases} 2\rho_{j+\frac{1}{2}} \ (u_{j+1} - u_j)^2 \ \dot{v} < 0 & \text{(compression)} \\ 0 \qquad\qquad\qquad\qquad\quad \dot{v} > 0 & \text{(expansion)} \ . \end{cases} \qquad \text{(B-9)}$$

The energy difference equations are solved by implicit Gauss-Seidel iteration as outlined in Richtmeyer.[20] The time step used was the minimum of Δt values required by the Courant condition, Δv/v and ΔT/T limits. Typically, 3500 calculational cycles were required per run. In a cycle, given the pressures, we advance the hydrodynamics and calculate the energy generated from burn, its transport and deposition. The energy equations are then iterated to solutions for the new temperatures, from which the new pressures are determined, in preparation for the next cycle.

II. NON-EQUILIBRIUM CODE

The second, non-equilibrium code, used to cross-check our results, has the same Lagrangian hydrodynamics, and ion and electron energy transport treatments, as above [Eq. (B-1) and Eqs. (B-2a,b)]. However, the term coupling the electrons to the radiation field, $A_{er}(T_e - T_r)$ in Eq. (B-2b), is modified, and the transport of radiation, neutrons and fast reaction products is accomplished by Monte Carlo simulation.

The application of standard Monte Carlo schemes to radiation transport is highly inefficient in high opacity regions where photons have a high probability of absorption close to their point of origin. Our code employs "a reduced source technique" which greatly improves the efficiency of particle simulation. The full radiation transport equation is

$$\left(\frac{1}{c}\frac{\partial}{\partial t} + \vec{\Omega}\cdot\vec{\nabla} + \frac{1}{\lambda_a} + \frac{1}{\lambda_s}\right)\phi(\nu,\Omega) -$$

$$\int A(\nu',\Omega' \rightarrow \nu,\Omega)\ \phi(\nu',\Omega')\ d\nu' d\Omega' \equiv$$

$$L(\phi) = S(\nu) = \frac{1}{\lambda_a} B(\nu) \quad , \qquad \text{(B-10)}$$

in which c is the speed of light, $\vec{\Omega}$ is a unit vector in the direction of the photon transported, dΩ is the differential solid angle around this direction, and φ is the radiation intensity (energy/time-area-frequency). The function S(ν) is the frequency ν dependent emission source. In fully ionized regimes, this is bremsstrahlung, which has the non-relativistic form

$$S(\nu) = \frac{4}{3\pi}\left(\frac{2}{\pi m_e kT_e}\right)^{\frac{1}{2}} \frac{\overline{Z}\ n_i^2\ \overline{Z^2}\ e^4}{hc} K_o\left(\frac{h\nu}{2kT_e}\right) e^{-\frac{h\nu}{kT_e}}$$

(en/time-volume-freq-steradian) , $\qquad$ (B-11)

and B(ν) is the Planckian distribution

$$B(\nu) = \frac{2h\nu^3}{c^2} \frac{1}{\left(e^{\frac{h\nu}{kT_e}} - 1\right)} \quad , \qquad \text{(B-12)}$$

which together define the absorption mean-free-path, corrected for stimulated emission, λ_a. Scattering is represented by the differential inverse Compton scattering length $A(\nu,\Omega \to \nu',\Omega')$, which is given analytically in Ref. 21. A first order relativistic approximation to the total Compton scattering length[21] is

$$\frac{1}{\lambda_s} \equiv \int A(\nu,\Omega \to \nu',\Omega')\, d\nu' d\Omega' \approx$$

$$\frac{8\pi}{3} \bar{Z}\, n_i r_o^2 \left\{ 1 - \frac{2h\nu}{mc^2} \left[\frac{K_1(\xi)}{K_2(\xi)} + \frac{4}{\xi} \right] \right\} \quad , \qquad \text{(B-13)}$$

containing r_o, the classical electron radius, and $\xi = mc^2/kT_e$. The K's are Bessel functions of the indicated order. The effects of material motion in Eq. (B-10) are neglected, so the source and cross-sections are isotropic.

To establish a "reduced source", we note that the left hand side of Eq. (B-10) is a linear operator acting on ϕ. Thus, if ϕ_e is an approximation to the true solution ϕ, then the deviation $\delta = \phi - \phi_e$ from the estimate obeys

$$L(\delta) = L(\phi) - L(\phi_e) = S - L(\phi_e) \equiv S_R \quad , \qquad \text{(B-14)}$$

which is Eq. (B-10), with $S(\nu)$ replaced by the reduced source S_R. Our procedure is to find a suitable estimated intensity ϕ_e by straightforward means, and then to solve for the intensity deviation δ by Monte Carlo simulation. Since the number of Monte Carlo "particles" required for an accurate simulation is proportional to the square of the source intensity, considerable computation time can be saved by the transport of δ, in lieu of ϕ, if ϕ_e is good enough so $\delta \ll \phi_e \approx \phi$ and $S_R \ll S$.

The estimate ϕ_e is found by replacing the kernel in Eq. (B-10) by an isotropic kernel that produces no frequency change (i.e., coherent scattering); $A(\nu,\Omega \to \nu',\Omega') \to \delta(\nu - \nu')/4\pi\lambda_s$. This gives for each frequency an equation of the form

$$\left(\frac{1}{c}\frac{\partial}{\partial t} + \mu \frac{\partial}{\partial r} + \frac{(1-\mu^2)}{r}\frac{\partial}{\partial \mu} + \frac{1}{\lambda_a} + \frac{1}{\lambda_s} \right) \phi_e -$$

$$\frac{1}{2\lambda_s} \int_{-1}^{+1} \phi_e(\mu')d\mu' = S(\nu) = \frac{1}{\lambda_a} B(\nu), \qquad \text{(B-15)}$$

which is reduced to spherical coordinates. The variable $\mu = \cos\theta$, where θ is the angle between the radius vector from the center of the pellet to a photon and the velocity vector of the photon. This equation is solved by the "spherical harmonic" method,[20] with truncation after the first Legendre Polynomial, i.e., with a "P_1 approximation". That is, the angular dependence is approximated by

$$\phi_e = \phi_o + \phi_1 \mu \quad . \qquad \text{(B-16)}$$

Equations for ϕ_o and ϕ_1 are obtained by taking the zeroeth and first moments of Eqs. (B-15,16) over μ; thus

$$\frac{1}{c}\frac{\partial \phi_o}{\partial t} + \frac{1}{3}\frac{\partial \phi_1}{\partial r} + \frac{2}{3}\frac{\phi_1}{r} + \frac{1}{\lambda_a}\phi_o = \frac{1}{\lambda_a} B(\nu) \qquad \text{(B-17a)}$$

$$\frac{1}{c}\frac{\partial \phi_1}{\partial t} + \frac{\partial \phi_o}{\partial r} + \left(\frac{1}{\lambda_s} + \frac{1}{\lambda_a} \right) \phi_1 = 0 \quad . \qquad \text{(B-17b)}$$

These equations are solved, semi-analytically, for a set of frequency groups, typically thirty. For each new advancement in time, the time derivatives are replaced by their difference form, eg.,

$$\frac{\partial \phi_o}{\partial t} \to \frac{\phi_o^{n+1} - \phi_o^{n}}{\Delta t_n} \quad , \quad \phi_o^{n}$$

is known, the remaining terms are associated with the n+1 time level, and exact ϕ_o^{n+1}, ϕ_1^{n+1} are found analytically across each zone, assuming constant λ_s, λ_a, and $B(\nu)$ within a zone. This relates the ϕ's at the zone boundaries, leading to exact solutions at these boundaries, by the inversion of a quad-diagonal matrix. With ϕ_e thus determined, the reduced source $S_R(\nu)$ for each frequency group is simply

$$S_R(\nu) = (1-\mu^2)\left[\frac{1}{\lambda_a}[B(\nu) - \phi_o] - \frac{\phi_1}{r} - \frac{1}{c}\frac{\partial \phi_o}{\partial t} \right]$$

$$- \frac{\phi_o}{\lambda_s} + \int \phi_o(\nu')\, a_o(\nu',\nu)d\nu' + \frac{2}{3}\mu \int \phi_1(\nu')\, a_1(\nu',\nu)d\nu' \qquad \text{(B-18)}$$

where $a_o(\nu',\nu) = \int A(\nu',\Omega' \to \nu,\Omega)\, d\Omega'$,

and $a_1(\nu',\nu) = \int A(\nu',\Omega' \to \nu,\Omega) \cos(\vec{\Omega}\cdot\vec{\Omega}')\, d\Omega'$.

For Thompson scattering, $a_1 \to 0$ and $a_o \to \delta(\nu-\nu')/\lambda_s$, so the lower line in Eq. (B-18) cancels. In high opacity regions, i.e., where $\ell/\lambda_a \ll 1$ (with ℓ the characteristic length of flow gradients), absorption dominates scattering, the radiation is nearly isotropic ($\phi_1 \ll \phi_o$), and slowly varying ($\partial\phi_o/\partial t \ll c/\lambda_a\, \phi_o$), so $S_R(\nu) \to (1-\mu^2)/\lambda_a\, (B(\nu) - \phi_o)$. Furthermore, by Eq. (B-17a,b), $\phi_o \to B(\nu)$, so, indeed $S_R \ll S$, and

$\delta \ll \phi_e$. In our $\rho = 3000$ g/cm^3, T = 3keV DT burn calculation, for example, $S_R/S \gtrsim 0.1$, allowing 10^2 fewer Monte Carlo particles for an accurate simulation.

Given that the solution ϕ ($\equiv \phi_e + \delta$) to Eq. (B-10) is obtained by the above methods, there is energy exchange with the electron field such that in Eq. (B-2b), the replacement

$$A_{e\nu}(T_r - T_e) \rightarrow \frac{4\pi}{\rho}\int \left(\frac{\phi - B(\nu)}{\lambda_a} + C(\nu)\phi\right) d\nu \ , \qquad \text{(B-19)}$$

should be made. Here

$$C(\nu) \equiv \int_0^\infty \frac{a_o(\nu',\nu)(\nu - \nu')}{\nu'} \, d\nu' \ .$$

The first term in Eq. (B-19) is the bremsstrahlung exchange; the second is the Compton energy transfer. At each time step $t = t^{n+1}$, Eqs. (B-2a,b) and Eq. (B-17a,b) are solved together implicitly, but with $\delta = \delta^n$ assumed, for T_e^{n+1}, T_i^{n+1}, and ϕ_e^{n+1}; then δ^{n+1} is determined explicitly by the Monte Carlo scheme.

With regard to the transport of the fast products from nuclear reactions, we note that scatterings are treated stochastically. Fast ion deposition into the field ions and electrons follows the Sec. III. a. prescription. The original fast particle sources are the D-D and D-T thermonuclear reactions. Additional fast particles are created by nuclear scatterings and "in-flight" reactions with field ions.

REFERENCES

1. J.S. Clarke, H.N. Fisher and R. J. Mason, Bull. Am. Phys. Soc. 17, 1035 (1972), Phys. Rev. Lett. 30, 89 (1973), and 30, 249 (1973).
2. J. Nuckolls, L. Wood, A. Thiessen, and G. Zimmerman, Nature (London) 239, 139 (1972).
3. N.G. Basov and O.N. Krohkin, Zh. Eksp. Teor. Fiz. 46, 171 (1964) [Sov. Phys. JETP 19, 123 (1964)].
4. J.M. Dawson, Phys. Fluids 7, 981 (1964).
5. W.J. Fader, Phys. Fluids 11, 2200 (1968).
6. R.R. Johnson and R.B. Hall, J. Appl. Phys. 42, 1035 (1971).
7. L. Spitzer, Physics of Fully Ionized Gases (Interscience, New York, 1969), Chap. V.
8. K. Boyer, Bull. Amer. Phys. Soc. 17, 1019 (1972), and Aeronautics and Astronautics 1, 28 (1973).
9. S. Glasstone and R.H. Loveberg, Controlled Thermonuclear Reactions (Van Nostrand, Princeton, N.J., 1960), p. 33.
10. J. L. Tuck, Nucl. Fusion 1, 202 (1961).
11. M.S. Chu, Phys. Fluids 15, 413 (1972).
12. C. Longmire, Elementary Plasma Physics (Wiley, New York, 1967), p. 203.
13. B.G. Carlson, LASL Report No. LA-1599, 1953, and R.D. Richtmeyer and K.W. Morton, "Difference Methods for Initial Value Problems," (Wiley, New York), p. 244.
14. Y.B. Zeldovich and Y.B. Raizer, Physics of Shock Waves and High Temperature Hydrodynamic Phenomena (Academic, New York, 1966) Vol. 1, p. 218.
15. H.N. Fisher, E.J. Linnebur, R.J. Mason, and R.L. Morse, Bull. Am. Phys. Soc. 18, 683 (1973).
16. A.L. Fuller and R.A. Gross, Phys. Fluids 11, 534 (1968).
17. A.F. Nastoyashchii and L.P. Shevehenko, At. Energ. 32, 451 (1972) [Sov. J. At. Energ. 32, 533 (1972)].
18. D.J. Hughes and R.B. Schwartz, "Neutron Cross Sections," Brookhaven National Laboratory Report No. 325, 2nd Edition (1958).
19. H. Hurwitz, (unpublished results).
20. R.D. Richtmeyer and K.W. Morton, "Difference Methods for Initial Value Problems," (Wiley, New York) Ch. 8 and 9.
21. G.S. Fraley, Los Alamos Scientific Laboratory Report No. LA-4592, (1971) (unpublished).